ADVANCED ENERGY MATERIALS
www.advenergymat.de

Perovskite Solar Cell Stability in Humid Air: Partially Reversible Phase Transitions in the PbI_2-CH_3NH_3I-H_2O System

*Zhaoning Song, Antonio Abate, Suneth C. Watthage, Geethika K. Liyanage, Adam B. Phillips, Ullrich Steiner, Michael Graetzel, and Michael J. Heben**

After rapid progress over the past five years, organic–inorganic perovskite solar cells (PSCs) currently exhibit photoconversion efficiencies comparable to the best commercially available photovoltaic technologies. However, instabilities in the materials and devices, primarily due to reactions with water, have kept PSCs from entering the marketplace. Here, laser beam induced current imaging is used to investigate the spatial and temporal evolution of the quantum efficiency of perovskite solar cells under controlled humidity conditions. Several interesting mechanistic aspects are revealed as the degradation proceeds along a four-stage process. Three of the four stages can be reversed, while the fourth stage leads to irreversible decomposition of the photoactive perovskite material. A series of reactions in the PbI_2-CH_3NH_3I-H_2O system explains the interplay between the interactions with water and the overall stability. Understanding of the degradation mechanisms of PSCs on a microscopic level gives insight into improving the long-term stability.

1. Introduction

Organic-inorganic perovskite solar cells (PSCs), mostly based on methylammonium lead iodide ($CH_3NH_3PbI_3$), have shown remarkable progress in the past five years. In addition to power conversion efficiencies exceeding 22%,[1] PSCs are easily processed and promise low manufacturing costs.[2,3] Consequently, PSCs are now considered as a viable alternative to other more established photovoltaic (PV) technologies such as crystalline Si, CdTe, and $CuIn_{1-x}Ga_xSe_2$. While these latter technologies have been successfully commercialized, large-scale deployment of PSCs is hindered by performance degradation. Although ≈4 months of stability have recently been demonstrated,[3] a 25–30 year lifetime is required to achieve a low levelized cost of energy which will allow PSCs to compete with other more established PV and conventional power generation technologies.

Tremendous effort has been devoted to understanding the decay mechanisms and developing appropriate solutions to improve PSC device stability.[3–5] Degradation can be due to humidity,[6] oxygen,[7] light,[8] and heat.[9] In nearly all studies, water has been implicated as a key culprit in causing instability in materials and devices. In early studies, the degradation of PSCs was attributed to hydrolysis reactions in which water molecules reacted with organic species in the parent material to drive decomposition and the release of gas phase HI and CH_3NH_2.[10] More recently, it has been revealed that hydrated perovskite phases, $CH_3NH_3PbI_3 \bullet H_2O$ and $(CH_3NH_3)_4PbI_6 \bullet 2H_2O$, may be formed during the initial degradation process.[11] Interestingly, the formation of the monohydrate phase can be fully reversed by exposing the hydrated perovskite to a dry environment.[11,12] To date, PSC degradation has been investigated by monitoring the current–voltage (J–V) behavior as a function of time under controlled temperature and humidity conditions.[4] Changes in the PV performance were correlated with general structural and compositional changes in the materials.[4] While instructive, this approach provides little information about the mechanisms and processes that control the causes and evolution of degradation on a microscopic level.

Recent advancements in imaging photocurrent, open circuit voltage, and recombination in thin-film solar cells with nano- and micro-scale resolution provide information on the performance of materials and devices[13] and their responses to environmental variation.[14] The understanding of the effects of spatially inhomogeneous chemical composition and crystallinity is particularly critical for designing strategies to improve the stability of PSCs. To elucidate the details of PSC failure mechanisms and develop pathways to produce stable devices, we performed in situ laser beam induced current (LBIC) mapping on state-of-the-art PSCs in the presence of moisture. Very

Z. Song, S. C. Watthage, G. K. Liyanage,
Prof. A. B. Phillips, Prof. M. J. Heben
Wright Center for Photovoltaics Innovation
and Commercialization
School for Solar and Advanced Renewable Energy
Department of Physics and Astronomy
University of Toledo
Toledo, Ohio 43606, United States
E-mail: Michael.Heben@utoledo.edu
Dr. A. Abate, Prof. U. Steiner
Adolphe Merkle Institute
Chemin des Verdiers 4, CH-1700 Fribourg, Switzerland
Dr. A. Abate, Prof. M. Graetzel
École Polytechnique Fédérale de Lausanne
Station 6, CH-1015 Lausanne, Switzerland

DOI: 10.1002/aenm.201600846

 © 2016 WILEY-VCH Verlag GmbH & Co. KGaA, Weinheim

few LBIC studies have been performed on PSCs to date,[14,15] and this is the first detailed LBIC investigation of perovskite degradation processes.

2. Results and Discussion

Spatially resolved external quantum efficiency (EQE) maps were obtained at 25 °C using LBIC (Figure S1, Supporting Information). The devices were ≈5 mm × 5 mm in size and were fabricated in the so-called n-i-p superstrate configuration on glass (see the Experimental Section). The initial device efficiencies were in the range of 16%–19%, as previously reported.[16] Each LBIC map was constructed by measuring the photogenerated current induced by a 40 micron wide 532 nm laser beam that was scanned across the device. The laser power was adjusted to be ≈0.01 mW to avoid heating. The measured current values were converted to EQE using a calibrated Si reference cell. EQE maps were measured in 6 min intervals and individual frames were assembled into videos that allow the temporal and spatial evolution of the LBIC signal to be visualized (Supporting Information). The PSCs were examined during exposure to the flowing N_2 gas containing moisture at relative humidity (RH) values of 50 ± 5% and 80 ± 5%.

The EQE maps in **Figure 1** show four distinct behaviors for devices exposed to a RH of 50% (1.6% H_2O in N_2). During Stage 1, the EQE of the PSCs increased slightly and peaked after a few minutes of exposure to humidity. During Stage 2, a rather uniform drop in photocurrent collection efficiency was observed over a time period of 18 to ≈105 min. Stage 3 is characterized by the propagation of a front that sweeps from the periphery of the device over ≈2 h and a dramatic reduction in the EQE. Stage 4 occurred more slowly and, surprisingly, displayed a temporary increase in the EQE at some locations in the device. Note that although variations from sample to sample were observed, all devices showed the same general behaviors.

A thorough analysis of the findings provides an understanding of the processes underlying each stage. In Stage 1, the EQE is not constant across the entire area even for these near-record devices (Figure 1a). Despite the fact that great care was taken to form uniform layers during processing, and to eliminate moisture during device manufacture (see the Experimental Section), defective areas are observed as well as significant spatial variation in the EQE from ≈60 to ≈80% in regions of the device that appear to be defect-free. Thus, there is significant potential for improving the performance of these devices simply by improving the uniformity of the current collection. For example, if the EQE across the entire area of the device was optimized to give the maximum value (83%), this particular 16.2% device would have an efficiency of 18.5%.

Although not easily discerned in the maps of Figure 1a, the spatially averaged EQE shown in the inset of Figure 1b exhibits a clear peak ≈5–10 min after the onset of humidity exposure. This somewhat surprising result can be explained by considering that recombination centers at the interface between spiro-OMeTAD and perovskite can be passivated by water molecules. Recently, it has been reported that uncoordinated ionic species on perovskite grain boundaries can be deactivated by hydrogen bonding with water, leading to reduced surface trap states

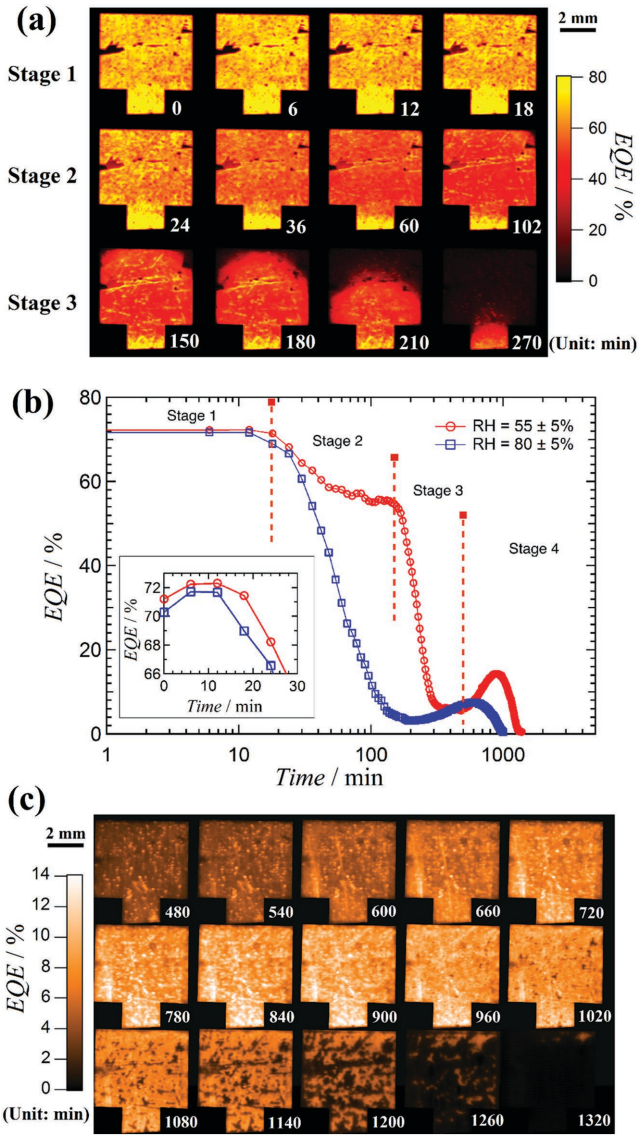

Figure 1. a) LBIC EQE maps (at 532 nm) of a typical perovskite solar cell after exposure to 50 ± 5% RH. b) Areal average LBIC EQE (at 532 nm) as a function of time after exposure to humidity. c) LBIC images for Stage 4 (480–1320 min) shown with a higher resolution color scale.

and better carrier extraction.[17] Water has also been found to improve the crystallinity and morphology of films during deposition, leading to better device performance.[18] In the present case, the devices were prepared under rigorously dry conditions and the performance rapidly improved upon exposure to water vapor. The route for water ingress could be diffusion along the pervoskite/spiro-OMeTAD interface from the edges of the device. Note that the gold back-contact is dense and continuous and, therefore, should be impervious to water.

The LBIC results of Stage 2 are characterized by a uniform decline in the photocurrent across the device. The EQE decreases quickly during the first hour, and then stabilizes before the onset of Stage 3. While the background EQE decreases, relatively large defects, such as the one seen at the left of the Stage 2 images in Figure 1a, may partially heal,

© 2016 WILEY-VCH Verlag GmbH & Co. KGaA, Weinheim

presumably due to passivation by water, as seen in Stage 1. Overall, the spatially averaged data in Figure 1b show that the EQE drops from ≈72% to ≈56% during Stage 2. To explain this we first consider that the conductivity in spiro-OMeTAD is produced by doping, which is achieved by oxidizing the molecular backbone.[19] In the present case, a lithium salt (e.g., lithium bis(trifluoromethanesulfonyl)imide) is used to promote an oxidative reaction between pristine spiro-OMeTAD and oxygen to produce mobile holes in the organic matrix.[19–21] Water incorporation has been shown to affect the electronic structure and hole mobility of doped spiro-OMeTAD in field effect transistor measurements,[22] so it is reasonable to expect water to impact the ability of spiro-OMeTAD to collect holes in the PV device configuration as well. The time constant for the phenomena responsible for Stage 2 is much slower than the time required for the Stage 1 enhancement, so the water transport mechanism is likely to be different. The spiro-OMeTAD layer has an amorphous structure and possesses internal channels that can efficiently transport O_2 and H_20,[4,21] but the rate of transport is evidently slower than the transport along the perovskite/spiro-OMeTAD interface. Because the degradation occurs in a rather uniform manner across the area of the device, the water concentration in the film at any time should also be uniform. To develop more insight, we performed optical transmission spectroscopy (Figure S2, Supporting Information) and observed changes in the optical transmittance that were consistent with water incorporation and a loss in the degree of oxidation of the spiro-OMeTAD.[20] Fourier transform infrared spectroscopy (FTIR) (Figure S3, Supporting Information) revealed reversible water-induced quenching of the NH^+ functionality that is indicative of hole conductivity. Consequently, it seems clear that the change in EQE can be ascribed to bulk changes in the doping state and hole collection efficiency of the spiro-OMeTAD layer.

After stabilizing at the end of Stage 2, Stage 3 commences at ≈105 min with a very large drop in EQE from ≈56% to a plateau at ≈6% where the EQE stabilizes once again. In contrast to Stages 1 and 2, Stage 3 degradation begins primarily at the top of the image and progresses downward (Figure 1a). In some cases, the degradation front propagates from the edges toward the center of the device (Figure S4, Supporting Information). The speed at which the degradation front spreads is determined by the humidity, regardless of whether the carrier gas is dry air or N_2, indicating that the degradation reaction is indeed related to the concentration gradient of water. With the capability to resolve the speed of propagation of the degradation front, which most likely corresponds to the rate of diffusion of water molecules in the perovskite film, degradation rates of 0.36 and 1.48 μm s^{-1} under 50% and 80% RH, respectively, were determined (Figure S5, Supporting Information).

The X-ray diffraction (XRD) results (Figure S6, Supporting Information) revealed that the dramatic EQE drop during Stage 3 is related to the formation of hydrated perovskite phases, consistent with other recent findings.[12] The intercalation of water molecules disrupts the long range order in the 3D perovskite structure by producing low-dimensional hydrated perovskites.[23] The development of degradation fronts for Stage 3 (Figure 1 and Figure S4) is a consequence of the creation of more efficient avenues for water transport in the active layer film as the $CH_3NH_3PbI_3 \bullet H_2O$ chains are formed. Figure S7 (Supporting Information) shows a schematic diagram of the cell as well as optical micrographs that show several of the device layers near a scribe line that is used to expose the front contact of the device for electrical connection. Evidently, Stage 3 response for the sample of Figure 1a is due to enhanced water ingress at the exposed $CH_3NH_3PbI_3$ surface. In situ J–V measurements (Figure S8, Supporting Information) shows that the formation of the monohydrated perovskite phase dramatically decreases the short circuit current (J_{SC}) and fill factor (FF) of the PSCs.

After the first three stages of degradation (≈330 min), the average EQE across the device was decreased from 71% to 6%, resulting in a completely failed device (Video S1, Supporting Information). These first three stages are, however, fully reversible (vide infra). These three stages, however, are followed by an irreversible fourth stage that has not yet been investigated in detail. During Stage 4, the average EQE begins to increase at ≈500 min from the Stage 3 plateau value of 6% to a maximum of ≈14% at 900 min. At longer times, the EQE then declines to 0% (Figure 1b). Video S2 (Supporting Information) clearly shows the microscopic changes during this stage of aging. Figure 1c shows the Stage 4 response with an increased EQE contrast. As the EQE begins to peak we see individual grains within the device becoming more effective at generating significantly higher photocurrents than the average for the cell. After ≈700 min, these spots increase in intensity (higher EQE), while the background currents decreased. The high intensity EQE at spots indicates that the material at specific locations is becoming more effective at photocurrent generation as the degradation proceeds, possibly due to disproportionation and phase separation to produce unhydrated perovskite grains and poorly photoactive materials such as perovskite hydrates or PbI_2. With continuing hydration (beginning at ≈930 min) these unhydrated perovskite grains are evidently consumed as well. Then, the inactive regions expand, leading to morphological changes and, subsequently, to complete device failure (at ≈1300 min). At this point, the color of the material has changed from dark brown to yellow (Figure S9, Supporting Information).

Stages 1 and 2 are clearly determined by the changes in charge carrier extraction (surface recombination) and transport (hole mobility) properties of the spiro-OMeTAD layer and the perovksite interfaces, suggesting possible improvements through the development of improved hole-transporting materials. Stages 3 and 4 are, on the other hand, related to reactions between water and the perovskite material and the resultant reactions and phase transformations. The hydration of perovskite responsible for Stage 3 behavior is a reversible reaction.[12] When the humidity is reduced, the metastable monohydrated perovskite phase loses crystalline water and converts back to $CH_3NH_3PbI_3$.[23] To investigate this reversibility with LBIC we mapped the photocurrent generation from devices subjected to hydration–dehydration cycles. **Figure 2**a shows images for the EQE recovery of a device that was hydrated under a RH of 80 ± 5% (3.4% water). Note that the higher humidity leads to a faster degradation rate (Figure 1b and Figure S10). In this case, the feature of Stage 2 cannot be separately distinguished due the rapid transition to Stage 3. This finding highlights that the rates of the two processes have different dependencies on the water concentration. When the atmosphere above

© 2016 WILEY-VCH Verlag GmbH & Co. KGaA, Weinheim

the device was subsequently purged with dry air for ≈4 h, the photocurrent completely recovered. Unlike the hydration which propagated along water diffusion pathways, the recovery of the photocurrent initiated at nuclei of recrystallized dehydrated perovskite grains and spread outward from there (Video S3, Supporting Information) as the photocurrent across the entire device increased gradually. The hydration–dehydration cycles were repeated several times without significant loss of current generation (Figure 2b). With multiple, deep hydration/dehydration cycles some degree of irreversibility begins to appear as defects form in the recrystallized $CH_3NH_3PbI_3$ grains. Under these conditions, morphological changes arise during the recrystallization of perovskite crystals (Figure S11, Supporting Information), along with permanent deterioration in the current generation.[24]

Note that the degradation caused by the hydration of $CH_3NH_3PbI_3$ is reversible only for the monohydrate phase that forms after short-time exposure to a low vapor pressure of water. Longer exposure times or exposures to higher H_2O vapor pressures can quickly lead to irreversible damage to the devices. Therefore, the Stage 4 degradation must consist of at least one irreversible reaction, most likely a water-catalyzed decomposition that leads to solid PbI_2 and volatile products.[10–12,24]

In general, the reactions between water and $CH_3NH_3PbI_3$ can be explained by a series of equilibria within the PbI_2-CH_3NH_3I-H_2O system (**Figure 3**). As described by Equations (1)–(4), four primary reactions can be considered: (a) the perovskite formation reaction, (b) the reversible formation of a monohydrated chain of perovskite, (c) the formation of dihydrated perovskites with reduced dimensionality, and (d) water-catalyzed decomposition to return to the starting components.

$$PbI_2 + CH_3NH_3I \Leftrightarrow CH_3NH_3PbI_3 \quad (1)$$

$$CH_3NH_3PbI_3 + H_2O \Leftrightarrow CH_3NH_3PbI_3 \cdot H_2O \quad (2)$$

$$(4-n)CH_3NH_3PbI_3 + n\,CH_3NH_3PbI_3 \cdot H_2O + (2-n)H_2O \Leftrightarrow (CH_3NH_3)_4\,PbI_6 \cdot 2H_2O + 3\,PbI_2 \quad (3)$$

$$(CH_3NH_3)_4\,PbI_6 \cdot 2H_2O \Leftrightarrow PbI_2 + 4\,CH_3NH_3I + 2H_2O \quad (4)$$

Equation (1) (Figure 3a) specifies the basic formation (forward) and thermal decomposition (reverse) reactions of stoichiometric $CH_3NH_3PbI_3$ in the absence of water. While there is a rather wide composition space for high efficiency pervoskite solar cells,[25] here we only consider the stoichiometric perovskite phase. When a low concentration of water is introduced into the system, perovskite crystals can react to form monohydrated chains through Equation (2) (illustrated in Figure 3b). The reverse reaction can be driven by a reduction in the partial pressure of water. Reaction between the monohydrate and dihydrated compounds occurs when the water vapor pressure is increased (Equation (3) and Figure 3c). The dimensional reduction from the 1D monohydrated chains to the 0D dihydrated perovskite phases requires the involvement of larger number of CH_3NH_3 cations, resulting in the formation of PbI_2 as a byproduct. This process redistributes organic and inorganic species, which causes an inhomogeneous composition, and alters the volume of the grains and the morphology of the film, and subsequently degrades the optoelectronic properties of the devices. Meanwhile, the excess ions ($CH_3NH_3^+$ and I^-) in the 0D dehydrated phase are able to migrate to neighboring locations containing PbI_2 nuclei, leading to the formation of $CH_3NH_3PbI_3$. Thus, certain locations in the film can participate in the actual formation reaction (Equation (1)) once again if the local water concentration is low. Under these conditions, individual $CH_3NH_3PbI_3$ grains can co-exist with hydrated phases and PbI_2 in locally phase separated regions. This phase separation likely accounts for the increase in photocurrent at local spots the in first part of Stage 4. If some of the reaction products are able to escape, the reaction becomes irreversible. For example, with gas flow removing CH_3NH_3I from the solid-state system, the reaction of Equation (4) moves to the right resulting in the irreversible formation of PbI_2 (Figure 3d). In support of this mechanism, we note that white CH_3NH_3I residue was found at the gas outlet of our environmental chamber after

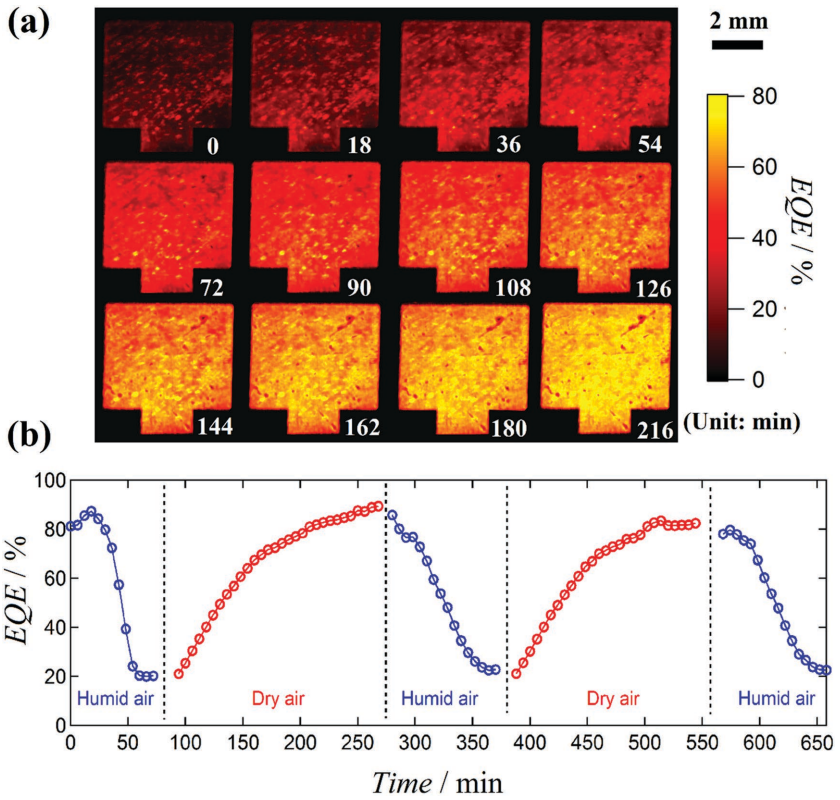

Figure 2. a) LBIC EQE maps of a hydrated perovskite device while purging with dry air. b) Areal average EQE (at 532 nm) of the perovskite device during hydration–dehydration cycles.

© 2016 WILEY-VCH Verlag GmbH & Co. KGaA, Weinheim

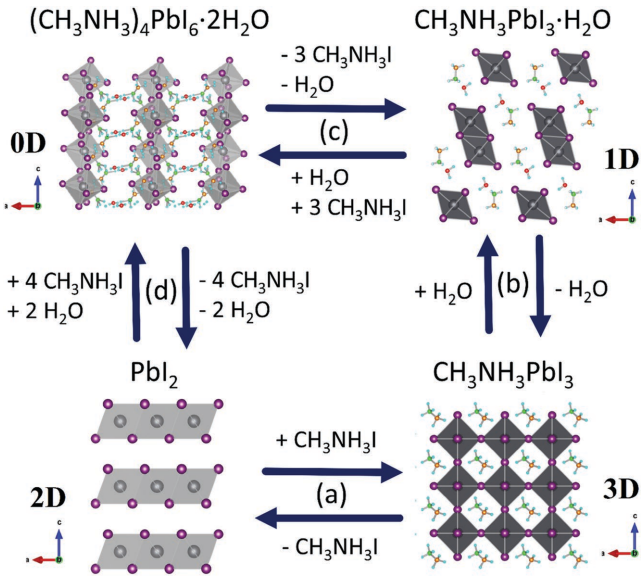

Figure 3. Schematic diagram of the phase equilibria in the PbI_2-CH_3NH_3I-H_2O system consisting of a) formation and decomposition of $CH_3NH_3PbI_3$, b) hydration and dehydration between the dry and monohydrated perovskites, c) equilibrium between mono- and dihydrated perovskites, and d) equilibrium between PbI_2, the dihydrate, CH_3NH_3I, and water.

≈30 devices were measured. As an aside, this suggests that CH_3NH_3I does not further decompose into CH_3NH_2 and HI in the presence of water as was suggested in early work,[10] which is consistent with reports of CH_3NH_3I stability in aqueous solutions.[26]

Understanding of the reactions in the PbI_2-CH_3NH_3I-H_2O system allows the stability of the perovskite thin films to be predicted under different conditions. However, the perovskite layers are very thin (≈300 nm) so the interfaces with the charge-transporting materials (TiO_2 and spiro-OMeTAD) could alter the kinetics and thermodynamics of the system's equilibria. To investigate the impact of the hole-transporting material on reaction between water and $CH_3NH_3PbI_3$, we compared the optical absorbance of two different film stacks, one with and one without a spiro-OMeTAD layer, at RH = 80% (the same conditions as in Figure 2). Surprisingly, the fluorine doped tin oxide (FTO)/TiO_2/$CH_3NH_3PbI_3$ sample was stable and exhibited no significant change in absorption at the perovskite band (≈1.6 eV) edge after 8 h (**Figure 4**a). From this result, it seems that the TiO_2 layer may render the perovskite film resistant to water uptake. This stability enhancement is likely due to the improved crystallinity of the perovskite film when deposited on the TiO_2 layer instead of a glass substrate. By contrast, the FTO/TiO_2/$CH_3NH_3PbI_3$/spiro-OMeTAD sample started to degrade immediately after water was introduced into the chamber (Figure 4b). Note that the loss of the band edge absorption is evidence for the formation of both mono and dihydrated perovskite species, both of which have a band gap above 3.1 eV.[12] In addition, the increased absorption of photons with energies <1.5 eV indicates the presence of water in the film stacks. Clearly, the presence of spiro-OMeTAD plays a role in accelerating the water ingress process and the decomposition of the perovskite material.

Although it has been reported that both spiro-OMeTAD itself and the hygroscopic Li-TFSI additive contribute to the instability of $CH_3NH_3PbI_3$,[11,27] the microscopic nature or origin of the accelerated degradation has not been clear. Combining the in situ LBIC and optical absorbance measurements makes it clear that the degradation is inhomogeneous (Figure 1c). We speculate that the internal channels within the hygroscopic spiro-OMeTAD layer may provide microenvironments of varying effective water concentration in contact with the perovskite films. This inhomogeneous water distribution would provide spatial variation that allowed partial or full hydration in some locations (Equations (2) and (3)), while other nearby environments with locally low H_2O concentrations could pull Equation (4) to the right which could in turn drive the $CH_3NH_3PbI_3$ formation reaction (Equation (1)). The fact that small molecules like H_2O and CH_3NH_3I can be freely transported in open channels within spiro-OMeTAD suggests that the microenvironments could be in communication with one another to support the behavior observed in Stage 4. This speculation is consistent with XRD data which show

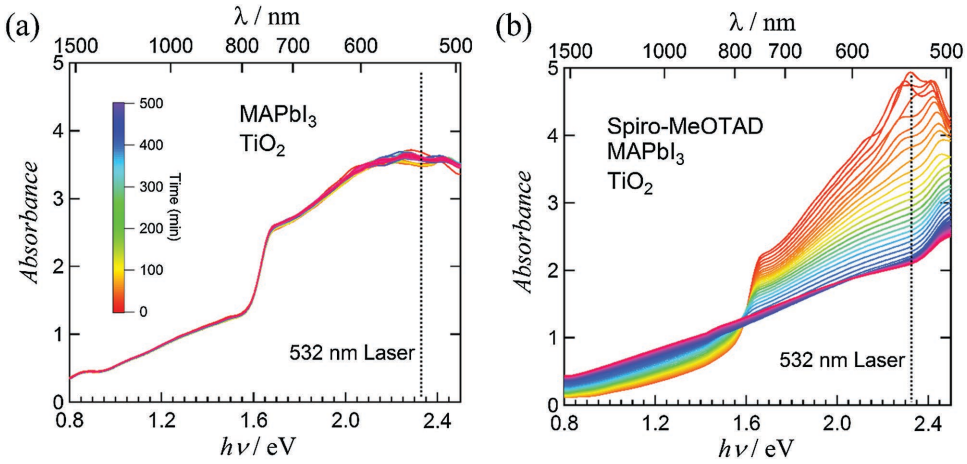

Figure 4. Optical absorbance spectra of a) FTO/TiO_2/$CH_3NH_3PbI_3$ and b) FTO/TiO_2/$CH_3NH_3PbI_3$/Spiro-OMeTAD aged under RH = 80%. The time between spectra is 12 min.

© 2016 WILEY-VCH Verlag GmbH & Co. KGaA, Weinheim

that the dihydrated phase is more likely to form when spiro-OMeTAD is present (Figure S6, Supporting Information).

The phase equilibria in the PbI_2-CH_3NH_3I-H_2O system provide a comprehensive understanding of the stability of $CH_3NH_3PbI_3$ in the presence of water, and, coupled with an understanding of water interactions with spiro-OMeTAD, can be used to understand device stability. To fabricate and maintain high efficiency devices it is critical to (1) reduce the water partial pressure to avoid the dimensional reduction from 1D monohydrate to 0D dihydrates, (2) avoid the use of hydroscopic materials in the device (e.g., spiro-OMeTAD), and (3) seal the device so that the volatile species cannot escape. Clearly, water impermeable encapsulation would provide an effective method to prepare devices with long-term stability. Note that devices are stable in dry air and exhibit no significant change in the EQE map after ≈1000 h (Figure S12, Supporting Information). However, due to the reversible nature of Stages 2 and 3, PSCs are compatible with processing in moderately humid air so long as the device is dried prior to encapsulation.

3. Conclusion

In summary, we have investigated the spatial evolution of the EQE during the exposure of perovskite solar cells to humid atmospheres using LBIC measurements. The results show that the device behavior proceeds through two stages that are controlled by water-induced carrier extraction and transport changes in the spiro-OMeTAD layer and two stages that are due to phase transformation in the perovskite material. The changes in solar cell performance are explained by both reversible and irreversible processes. On the basis of these observations, we propose phase equilibria within the PbI_2-CH_3NH_3I-H_2O system to understand the water-induced degradation, and suggest that a dehydration process before device encapsulation will potentially improve the stability of perovskite solar cells.

4. Experimental Section

General Methods: All the synthetic procedures and the device fabrications were carried out under a nitrogen atmosphere. All reagents and solvents were purchased from commercial sources and used without further purification unless otherwise noted.

Solar Cells Fabrication: Devices were fabricated on FTO coated glass substrates. The substrates were cleaned sequentially with Hellmanex soap in an ultrasonic bath for 30 min, then washed with acetone, isopropanol and finally cleaned in an oxygen plasma for 5 min. An ≈30 nm thick TiO_2 compact layer was deposited on FTO by spray pyrolysis at 450 °C from a precursor solution prepared with acetil acetone (0.4 mL, Aldrich), titanium diisopropoxide bis(acetylacetonate) solution (0.6 mL, 75% in 2-propanol, Aldrich), and ethanol (9 mL). After spraying, the substrates were left at 450 °C for 5 min, and were then left to cool down to room temperature. A mesoporous TiO_2 layer was deposited by spin coating for 10 s at 4000 rpm with a ramp of 2000 rpm s^{-1}, using 30 nm particle paste (Dyesol) diluted in ethanol to achieve about 150 nm thick layer. After spin coating, the substrate was immediately dried at 100 °C for 10 min and then sintered again at 500 °C for 30 min, under dry air flow. Mesoporous TiO_2 was doped with lithium by spin coating a solution of bis(trifluoromethanesulfonyl)imide (Li-TFSI, 0.1 M, Aldrich) in acetonitrile at 3000 rpm for 30 s.[16] After spin coating, the substrate was immediately dried at 100 °C for 10 min and then sintered again at 500 °C for 30 min, under dry air flow. After cooling down to 150 °C, the substrates were immediately transferred into a nitrogen atmosphere glove box for depositing the perovskite films.

The perovskite films were deposited from a precursor solution containing methylammonium iodide (1.1 M) and lead iodide (1.2 M) in anhydrous dimethylformamide (DMF):dimethyl solfoxide (DMSO) 4:1 (v:v). The perovskite solution was spin coated in two steps, at 1000 and 4000 rpm for 10 and 30 s, respectively. During the second step, clorobenzene (100 µL) was poured on the spinning substrate 15 s prior to the end of the program. The substrates were then annealed at 100 °C for 1 h in the nitrogen-filled glove box.

After the perovskite annealing the substrates were cooled down for few minutes and a spirofluorene linked methoxy triphenylamines (spiro-OMeTAD, Merck) solution was spun on at 4000 rpm for 20 s. The spiro-OMeTAD solution (0.07 M) was prepared in chlorobenzene, and doped with Li-TFSI (50 mol%) from a stock solution of Li-TFSI (1.8 M) in acetonitrile, tert-butylpyridine (tBP, 330 mol%, Aldrich) and Tris(2-(1H-pyrazol-1-yl)-4-tert-butylpyridine)- cobalt(III) Tris(bis(trifluoromethylsulfonyl)imide) (Co-complex, 3 mol%, Dyesol) from a stock solution Co-complex (0.25 M) in acetonitrile.[19,28] Finally, 80 nm of gold was deposited by thermal evaporation under high vacuum, using a shadow masking to pattern the electrode.

LBIC Measurements: An LBIC system built in house was used to spatially resolve the current collection efficiency map.[13] A 532 nm Nd:YAG laser operating in the Q-switching mode at a repetition rate of 600 kHz was used to generate a light beam with an average power of 0.01 mW and a 40 µm diameter (corresponding to a power density of ≈800 mW cm^{-2} or 2.14×10^{18} photons s^{-1} cm^{-2}). Computer controlled over-head galvanometers were used to scan the laser beam across the solar cells at a speed of 1 mm s^{-1} with a 30 µm spacing between two lateral scans. The scanning area of an LBIC map was 8 mm by 8 mm. Individual devices were isolated by an electronic switch (Keithley 7001) and connected to a Keithley 2601 source meter. Light-induced current signals were collected at an acquisition rate of 5 kHz and converted into local external quantum efficiencies using a reference Si photodiode (Model: S2281-8D083) with a calibrated EQE (Figure S13, Supporting Information).

In Situ LBIC Measurement: An airtight environmental box (Figure S10, Supporting Information) was built to study the degradation of perovskite solar cells in humidity. The box was purged with a carrier gas (dry air or N_2) through a water bubbler at a flow rate of 3 standard cubic feet per hour (SCFH) (0.083 m^3 min^{-1}). The gas bubbler was kept at 30 and 60 °C to maintain a 50 ± 5% and 80 ± 5% RH, respectively. The RH value was monitored by a commercial hygrometer stored in an airtight container that connected to the outlet of the environmental box. Time resolved LBIC maps were collected in 6 min intervals to study the evolution of the device degradation. A total of eight devices are discussed in this report, four of which were examined under 50% RH and four that were examined under 80% RH. The behavior was repeatable under each environmental condition, and consistent with other measurements that are not part of this study.

In Situ Current–Voltage Measurement: J–V measurements were recorded using a Keithley 2440 source meter and a solar simulator (Newport model 91195A-1000). A calibrated Si photodiode was used to configured the light intensity to simulate AM1.5 illumination. The environmental conditions were controlled in the same way as in the LBIC measurement. Time resolved *J–V* curves were measured from 1.2 to 0 V at a sweep speed of 0.2 V s^{-1} in 12 min intervals.

Thin Film Stack Preparation: Thin films stacks of FTO/TiO_2/$CH_3NH_3PbI_3$ and FTO/TiO_2/$CH_3NH_3PbI_3$/spiro-OMeTAD were prepared following the same recipe as in the solar cells fabrication section, with the exception of the spiro-OMeTAD film, which contained Li-TFSI and tBP additives, but not the Co-complex. The spiro-OMeTAD film used for FTIR measurement was spin-coated on a sapphire substrate.

In Situ Optical Measurement: An environmental chamber (Figure S10, Supporting Information) was built to study the evolution of optical properties of the thin films stacks in humidity. Time resolved optical spectra were recorded by a spectrophotometer (Perkin Elmer

© 2016 WILEY-VCH Verlag GmbH & Co. KGaA, Weinheim

Lambda 1050) in the range of 350–2200 nm in 12 min intervals. The humidity conditions were controlled in the same method of the LBIC measurement. The extinction coefficient was calculated by $k = \lambda A/4\pi d$, where λ is the wavelength, A is optical absorbance, and d is the thickness of the film stack.

Other Characterization Methods: An FTIR spectrometer (Nicolet 6700, Thermo Fisher Scientific) was used to measure the Fourier transform infrared spectroscopic spectra of spiro-OMeTAD films in the attenuated total reflection mode. The spectra were recorded with a 1 cm^{-1} resolution. An X-ray diffractometer (Rigaku Ultima III) was used to measure XRD spectra of the film stacks in the range from 5° to 60° with a step size of 0.02° and a speed of 0.50° per minute. A field emission scanning electron microscope (Hitachi S-4800) was used to acquire scanning electron microscopy (SEM) images of aged devices.

Supporting Information

Supporting Information is available from the Wiley Online Library or from the author.

Acknowledgements

Z. S., S. W., G. L., A. P., and M. H. were supported by the Air Force Research Laboratory, Space Vehicles Directorate (Contract No. FA9453-11-C-0253) and the National Science Foundation (Contract No. CHE-1230246). A. A. had received funding from the European Union's Seventh Framework Programme for research, technological development and demonstration under grant agreement no. 291771. A. A., U. S., and M. G. acknowledge funding by the Swiss National Science Foundation through the NRP70 program.

Received: April 22, 2016
Revised: May 24, 2016
Published online:

[1] NREL, Solar Efficiency Chart, http://www.nrel.gov/ncpv/images/efficiency_chart.jpg (accessed: April 2016).
[2] a) P. Gao, M. Gratzel, M. K. Nazeeruddin, *Energy Environ. Sci.* **2014**, *7*, 2448; b) Z. Song, S. C. Watthage, A. B. Phillips, M. J. Heben, *J. Photon. Energy* **2016**, *6*, 022001; c) S. D. Stranks, H. J. Snaith, *Nat. Nanotechnol.* **2015**, *10*, 391.
[3] T. Leijtens, G. E. Eperon, N. K. Noel, S. N. Habisreutinger, A. Petrozza, H. J. Snaith, *Adv. Energy Mater.* **2015**, *5*, 1500963.
[4] T. A. Berhe, W.-N. Su, C.-H. Chen, C.-J. Pan, J.-H. Cheng, H.-M. Chen, M.-C. Tsai, L.-Y. Chen, A. A. Dubale, B.-J. Hwang, *Energy Environ. Sci.* **2016**, *9*, 323.
[5] Q. Chen, N. De Marco, Y. Yang, T.-B. Song, C.-C. Chen, H. Zhao, Z. Hong, H. Zhou, Y. Yang, *Nano Today* **2015**, *10*, 355.
[6] Y. Han, S. Meyer, Y. Dkhissi, K. Weber, J. M. Pringle, U. Bach, L. Spiccia, Y.-B. Cheng, *J. Mater. Chem. A* **2015**, *3*, 8139.
[7] N. Aristidou, I. Sanchez-Molina, T. Chotchuangchutchaval, M. Brown, L. Martinez, T. Rath, S. A. Haque, *Angew. Chem. Int. Ed.* **2015**, *54*, 8208.
[8] T. Leijtens, G. E. Eperon, S. Pathak, A. Abate, M. M. Lee, H. J. Snaith, *Nat. Commun.* **2013**, *4*, 2885.
[9] G. Divitini, S. Cacovich, F. Matteocci, L. Cinà, A. Di Carlo, C. Ducati, *Nat. Energy* **2016**, *1*, 15012.
[10] J. M. Frost, K. T. Butler, F. Brivio, C. H. Hendon, M. van Schilfgaarde, A. Walsh, *Nano Lett.* **2014**, *14*, 2584.
[11] J. Yang, B. D. Siempelkamp, D. Liu, T. L. Kelly, *ACS Nano* **2015**, *9*, 1955.
[12] A. M. A. Leguy, Y. Hu, M. Campoy-Quiles, M. I. Alonso, O. J. Weber, P. Azarhoosh, M. van Schilfgaarde, M. T. Weller, T. Bein, J. Nelson, P. Docampo, P. R. F. Barnes, *Chem. Mater.* **2015**, *27*, 3397.
[13] a) M. S. Leite, M. Abashin, H. J. Lezec, A. Gianfrancesco, A. A. Talin, N. B. Zhitenev, *ACS Nano* **2014**, *8*, 11883; b) U. W. Paetzold, S. Lehnen, K. Bittkau, U. Rau, R. Carius, *Nano Lett.* **2014**, *14*, 6599; c) M. Vrućnić, C. Matthiesen, A. Sadhanala, G. Divitini, S. Cacovich, S. E. Dutton, C. Ducati, M. Atatüre, H. Snaith, R. H. Friend, H. Sirringhaus, F. Deschler, *Adv. Sci.* **2015**, *2*, 1500136; d) E. M. Tennyson, J. L. Garrett, J. A. Frantz, J. D. Myers, R. Y. Bekele, J. S. Sanghera, J. N. Munday, M. S. Leite, *Adv. Energy Mater.* **2015**, *5*, 1501142; e) Y. Kutes, B. A. Aguirre, J. L. Bosse, J. L. Cruz-Campa, D. Zubia, B. D. Huey, *Prog. Photovoltaics* **2016**, *24*, 315; f) Y. Galagan, B. Zimmermann, E. W. C. Coenen, M. Jørgensen, D. M. Tanenbaum, F. C. Krebs, H. Gorter, S. Sabik, L. H. Slooff, S. C. Veenstra, J. M. Kroon, R. Andriessen, *Adv. Energy Mater.* **2012**, *2*, 103; g) J. R. Sites, T. J. Nagle, in *31st Photovoltaic Specialists Conference (PVSC)*, IEEE, Lake Buena Vista, FL, United States **2005**, DOI: 10.1109/PVSC.2005.1488104.
[14] a) Z. Song, S. C. Watthage, B. L. Tompkins, G. K. Liyanage, A. B. Phillips, R. J. Ellingson, M. J. Heben, in *42nd Photovoltaic Specialist Conference (PVSC)*, IEEE, New Orleans, LA, United States **2015**, DOI: 10.1109/PVSC.2015.7355676; b) Z. Song, S. C. Watthage, A. B. Phillips, G. K. Liyanage, R. R. Khanal, B. L. Tompkins, R. J. Ellingson, M. J. Heben, *Proc. SPIE* **2015**, *9561*, 956107.
[15] S. Mastroianni, F. D. Heinz, J. H. Im, W. Veurman, M. Padilla, M. C. Schubert, U. Wurfel, M. Gratzel, N. G. Park, A. Hinsch, *Nanoscale* **2015**, *7*, 19653.
[16] a) F. Giordano, A. Abate, J. P. Correa Baena, M. Saliba, T. Matsui, S. H. Im, S. M. Zakeeruddin, M. K. Nazeeruddin, A. Hagfeldt, M. Graetzel, *Nat. Commun.* **2016**, *7*, 10379; b) D. Bi, W. Tress, M. I. Dar, P. Gao, J. Luo, C. Renevier, K. Schenk, A. Abate, F. Giordano, J.-P. Correa Baena, J.-D. Decoppet, S. M. Zakeeruddin, M. K. Nazeeruddin, M. Grätzel, A. Hagfeldt, *Sci. Adv.* **2016**, *2*, 1501170.
[17] W. Zhou, Y. Zhao, C. Shi, H. Huang, J. Wei, R. Fu, K. Liu, D. Yu, Q. Zhao, *J. Mater. Chem. C* **2016**, *120*, 4759.
[18] G. E. Eperon, S. N. Habisreutinger, T. Leijtens, B. J. Bruijnaers, J. J. van Franeker, D. W. deQuilettes, S. Pathak, R. J. Sutton, G. Grancini, D. S. Ginger, R. A. J. Janssen, A. Petrozza, H. J. Snaith, *ACS Nano* **2015**, *9*, 9380.
[19] A. Abate, T. Leijtens, S. Pathak, J. Teuscher, R. Avolio, M. E. Errico, J. Kirkpatrik, J. M. Ball, P. Docampo, I. McPherson, H. J. Snaith, *Phys. Chem. Chem. Phys.* **2013**, *15*, 2572.
[20] U. B. Cappel, T. Daeneke, U. Bach, *Nano Lett.* **2012**, *12*, 4925.
[21] Z. Hawash, L. K. Ono, S. R. Raga, M. V. Lee, Y. Qi, *Chem. Mater.* **2015**, *27*, 562.
[22] a) L. K. Ono, P. Schulz, J. J. Endres, G. O. Nikiforov, Y. Kato, A. Kahn, Y. Qi, *J. Phys. Chem. Lett.* **2014**, *5*, 1374; b) S. Fantacci, F. De Angelis, M. K. Nazeeruddin, M. Grätzel, *J. Mater. Chem. C* **2011**, *115*, 23126.
[23] F. Hao, C. C. Stoumpos, Z. Liu, R. P. H. Chang, M. G. Kanatzidis, *J. Am. Chem. Soc.* **2014**, *136*, 16411.
[24] J. A. Christians, P. A. Miranda Herrera, P. V. Kamat, *J. Am. Chem. Soc.* **2015**, *137*, 1530.
[25] Z. Song, S. C. Watthage, A. B. Phillips, B. L. Tompkins, R. J. Ellingson, M. J. Heben, *Chem. Mater.* **2015**, *27*, 4612.
[26] J. Zhao, B. Cai, Z. Luo, Y. Dong, Y. Zhang, H. Xu, B. Hong, Y. Yang, L. Li, W. Zhang, C. Gao, *Sci. Rep.* **2016**, *6*, 21976.
[27] L. Zheng, Y.-H. Chung, Y. Ma, L. Zhang, L. Xiao, Z. Chen, S. Wang, B. Qu, Q. Gong, *Chem. Commun.* **2014**, *50*, 11196.
[28] A. Abate, D. R. Staff, D. J. Hollman, H. J. Snaith, A. B. Walker, *Phys. Chem. Chem. Phys.* **2014**, *16*, 1132.

© 2016 WILEY-VCH Verlag GmbH & Co. KGaA, Weinheim